Article

MoS$_2$-Cu/CuO@graphene Heterogeneous Photocatalysis for Enhanced Photocatalytic Degradation of MB from Water

Asim Jilani [1],* and **Ammar A. Melaibari [1,2]**

1   Center of Nanotechnology, King Abdulaziz University, Jeddah 21589, Saudi Arabia
2   Department of Mechanical Engineering, King Abdulaziz University, Jeddah 21589, Saudi Arabia
*   Correspondence: asim.jilane@gmail.com or ajilani@kau.edu.sa

Abstract: The industrial revolution resulted in the contamination of natural water resources. Therefore, it is necessary to save and recover the natural water resources. In this regard, polymer-based composites have attracted the scientific community for their application in wastewater treatment. Herein, molybdenum disulfide composites with a mix phase of copper, copper oxide and graphene (MoS$_2$-Cu/CuO@GN) were synthesized through the hydrothermal method. Methylene blue (MB) was degraded by around 93.8% within the 30 min in the presence of MoS$_2$-Cu/CuO@GN under visible light. The degradation efficiency was further enhanced to 98.5% with the addition of H$_2$O$_2$ as a catalyst. The photocatalytic degradation efficiency of pure MoS$_2$, MoS$_2$-Cu/CuO and MoS$_2$-Cu/CuO@GN were also investigated under the same experimental conditions. The structural analysis endorses the presence of the Cu/CuO dual phase in MoS$_2$. The charge recombination ratio and band gap of MoS$_2$-Cu/CuO@GN were also investigated in comparison to pure MoS$_2$ and MoS$_2$-Cu/CuO. The chemical states, the analysis of C1s, O1s, Mo3d and Cu2p3, were also analyzed to explore the possible interaction among the present elements. The surface morphology confirms the existence of Cu/CuO and GN to MoS$_2$.

Keywords: photocatalysis; dye degradation; MoS$_2$; graphene supported catalysts; water cleaning

1. Introduction

Environmental and energy remediation are two major issues for human beings due to rapid industrialization [1]. The rapid increase in industrialization activities resulted in the contamination of natural water resources. The organic dyes and various kinds of heavy metals are being discharged into water reservoirs on a daily basis from different industrial activities [2]. These contaminations in water are a severe threat for human health and the ecosystem. In this regard, various materials and methods have been deployed to remove the contamination from the water, such as absorption, membrane filtration and photocatalytics [3]. However, the photocatalytic process is being considered an efficient and cost-effective way to remove or neutralize hazardous material from water [4]. Therefore, various materials such as carbon-based metals and metals oxides and, more importantly, polymers are attractive candidates to remove the pollutants through the photocatalytic process [5].

Polymers are among the most versatile materials for wastewater treatment through photocatalysts, membranes and the absorption process owing to chemical stability/versatility, ease of functionalization, high specific surface, etc., [6,7]. Therefore, a two-dimensional-layered structure of molybdenum disulfide (MoS$_2$) has attracted the scientific community because of its extraordinary structure and properties such as strong oxidizing activity, non-toxicity in nature and a low band gap (1.8 eV) that can be further tuned with quantum confinement effects [8]. This low band gap of the MoS$_2$ is beneficial to absorb the light photons in the visible region which is highly desirable to enhance the photocatalytic process [9,10]. However, the interaction of Mo–S can engender the unsaturated atoms at

the crystal edge which may render the photocatalytic activity of MoS_2 [11]. Therefore, the doping of some metals or metal oxides can enhance the photocatalytic activity of MoS_2.

In this context, p-type semiconductor materials such as copper oxide (CuO) have gained attention due to their photo-conductivity nature, which supports enhancing the photocatalytic activity of n-type MoS_2 by reducing the charge recombination ratio [12]. Moreover, CuO doping can enhance the absorption of light photons which results in the augmentation of catalytic activity [13]. Further the mix phase of Cu/CuO supports the formation of heterojunction which reduces the recombination of charge carriers that can enhance the photocatalytic activity [14]. However, the access amount of CuO in composites can provide the recombination center for charge carriers which will reduce the photocatalytic activity [15]. Therefore, the optimal amount of CuO is also important to enhance photocatalytic activity.

The charge carrier separation can be enhanced by the addition of graphene (GN) which amended the charge separation and absorbed the more visible light which consequently enhanced the photocatalytic activity [16]. Moreover, GN can also create some defects while making the composites with metals and metal oxides. These defects can capture the pollutant during the photocatalytic process [17] which makes it attractive for wastewater treatment. Further, the high specific surface area (2650 m^2/g), π orbital, π–π interaction, functional groups makes it an attractive dopant with metal, metal oxides and polymers to synthesiss the photocatalysts [18].

Previous studies show that there are various reports on MoS_2 with GN and CuO and other metal oxides as a catalyst [12,19,20]. However, the low catalytic performance is still a major issue for these binary composites. Further, there are few reports on the role of metals and metal oxides in the photocatalytic activity of MoS_2. Therefore, in this study, the combination of MoS_2 with GN and Cu/CuO mix phases were synthesized through an in-suit hydrothermal process. The role of Cu/CuO and GN to enhance the photocatalytic activity of MoS_2 was explored. Moreover, the change in the functional groups through XPS and the change in optical and structural properties were also studied.

2. Experimental Section

2.1. Materials

Molybdenum (VI) oxide (99.97%), thiourea ($\geq$99.0%), copper (II) sulfate ($\geq$99.99%), CTAB ($\geq$99.0%), ascorbic acid ($\geq$99.0%), sodium hydroxide ($\geq$98.0%), graphite powder ($\geq$99.99%), sulfuric acid (95 to 98%) and methylene blue (80%) were purchased from Sigma Aldrich Burlington USA and used for the synthesis of MoS_2-Cu/CuO@GN without any further treatment.

2.2. Synthesis of MoS_2-Cu/CuO@GN

MoS_2 was synthesized by hydrothermal methodology using MoO_3 and thiourea as precursors. In a typical process, 0.1150 g of MoO_3 and 0.2664 g of thiourea was taken in 80 mL of water and the system was put under stirring conditions for 30 min. Thereafter, the whole reaction mixture was transferred to 100 mL of Teflon-lined hydrothermal reactor and subsequently heated at 200 °C for 24 hrs. Thus, obtained the black precipitate of MoS_2 was separated by centrifugation, washed with excess of water and ethanol, dried at 80 °C for 12 h and subsequently stored in desiccator for further experiments.

For the MoS_2-Cu/CuO@GN, first, binary composite of MoS_2-Cu/CuO was prepared and further coating of GN over it resulted in MoS_2-Cu/CuO@GN. The GO (stock solution of 10 mg/mL) and Cu/CuO nanoparticles were prepared separately. The synthesis of GO can be seen elsewhere [21]. The Cu/CuO nanoparticles were synthesized by the reduction of copper (II) sulfate in the presence of CTAB surfactant. In a typical process, 0.1 M copper (II) sulfate solution was dissolved in 100 mL of water and to it, 0.25 g of CTAB was added and the whole system was put under stirring conditions. In another beaker, 50 mL of 0.2 M ascorbic acid solution was prepared. In the second step, the solution of ascorbic acid was slowly added to the copper (II) sulfate solution and, subsequently, 30 mL of 1 M

sodium hydroxide solution was also added. The whole system was heated to 80 °C for 2 h and a dark reddish–brown color confirmed the formation of Cu/CuO. Thus, prepared Cu/CuO was separated by centrifugation, washed with excess of water and ethanol and subsequently dried at room temperature [22]. The MoS_2-Cu/CuO was prepared by mixing 1 g of MoS_2 and 0.1 g of Cu/CuO in 50 mL ethanol and the mixture was put in ultrasonic bath for 1 h, followed by stirring on hot plate until the complete evaporation of ethanol. Further, the fabrication of ternary MoS_2-Cu/CuO@GN was done by mixing 10 mL of GO with 1 g of MoS_2-Cu/CuO and the whole mixture was heated at 400 °C for 3 h for the complete reduction of GO into GN and to, subsequently, give MoS_2-Cu/CuO@GN. The ratios of MoS_2, Cu/CuO and GN were, respectively, 87.1%, 8.71 and 4.19%.

2.3. Photodegradation Measurement

MB was selected as model pollutant to assess the catalytic performance of MoS_2, MoS_2-Cu/CuO and MoS_2-Cu/CuO@GN. In this regard, 25 mg of catalyst (optimized against initial concentration of MoS_2 and pH Figure S1) was added to the 20 ppm aqueous solution of MB. However, the MB solution containing the catalyst was put in the dark under vigorous stirring for 30 min to achieve the adsorption desorption equilibrium. Afterwards, the solution was irradiated with visible light of 2 watt, having a distance of 12 cm from MB solution for 30 min. The intensity was approximately 11.06 watt/meter. During this irradiation, a certain amount (5 mL) of solution was taken to estimate the degradation of MB by measuring the spectrum through UV-Visible spectrometer.

The MB degradation ability of prepared photocatalysts was calculated by applying the following relation [23]:

$$Degradation\ (\%) = \left(\frac{C_o - C_t}{C_o} \right) 100 \tag{1}$$

where C_o represent the initial taken concentration of MB while C_t symbolizes the remaining MB concentration after interval of 10 min. Once the photocatalytic efficiency was calculated, then following giving relation was used to calculate the reaction rate constant during degradation process [24].

$$\ln(\frac{C}{C_o}) = -kt \tag{2}$$

2.4. Characterizations

The structural and surface compositional analysis of MoS_2, MoS_2-Cu/CuO and MoS_2-Cu/CuO@GN were performed, respectively, with X-ray diffraction (Ultima IV-Rigaku Tokyo Japan) and X-ray photoelectron spectroscopy (PHI-Versa ProbeII Chanhassen USA). The pass energies of 187.85 eV and 47.46.95 eV were used, respectively, to acquire the survey and narrow scan mode. Surface morphology was investigated by field emission scanning electron microscopy (JSM7600-F-Jeol Tokyo Japan). The spectrometer (DR 6000 Hach Loveland USA) was used to calculate the absorption of MB, while charge recombination ratio was investigated through photoluminescence spectrometer (Shimadzu RF 5301PC Kyoto Japan).

3. Results and Discussion

3.1. Structural Analysis

The diffraction analysis of MoS_2, MoS_2-Cu/CuO and MoS_2-Cu/CuO@GN (Figure 1) reveals the clear diffraction peaks which are attributed to the crystalline nature of synthesized photocatalysts. The diffraction pattern of pure MoS_2 revealed the diffraction peak around 2θ = 14.27, 33.04 and 61.65 which, respectively, attributed to the diffraction planes, (002), (100) and (1007), of the molybdenite-2H phase (JCPD #00-037-1492). The addition of Cu/CuO to MoS_2 (MoS_2-Cu/CuO) resulted in enhancing the sharp diffraction pattern with some additional new diffraction peaks in comparison to the pure MoS_2 diffraction

pattern. The additional diffraction appeared around 2θ = 36.59, 38.98, 43.43, 50.56, 61.65 and 74.20. The diffraction peaks at 2θ = 36.59, 38.98 and 61.65 are attributed to the tenorite phase of CuO (JCPD # 00-001-1117), while the diffraction peaks at 2θ = 43.43, 50.56 and 74.20 are the representation of copper (Cu), as revealed in JCPD # 01-085-1326. Therefore, XRD analysis confirms the presence of Cu/CuO with MoS$_2$. Moreover, after the addition of GN (MoS$_2$-Cu/CuO@GN), no additional peak was observed. The non-observable diffraction peak of GN is attributed due to the exfoliation nature [25]. Further, the functional groups of GN can interact with MoS$_2$ and Cu/CuO may lead to variations in the structural properties without changing the preferred orientation of the diffraction planes [26]. This could be noticed in our diffraction analysis (Table 1) that shows the change in the crystal grain size, which also revealed the successful interaction of GN functional groups with MoS$_2$ and Cu/CuO. The Scherrer relation was used to estimate the crystal size of MoS$_2$, MoS$_2$-Cu/CuO and MoS$_2$-Cu/CuO@GN [27].
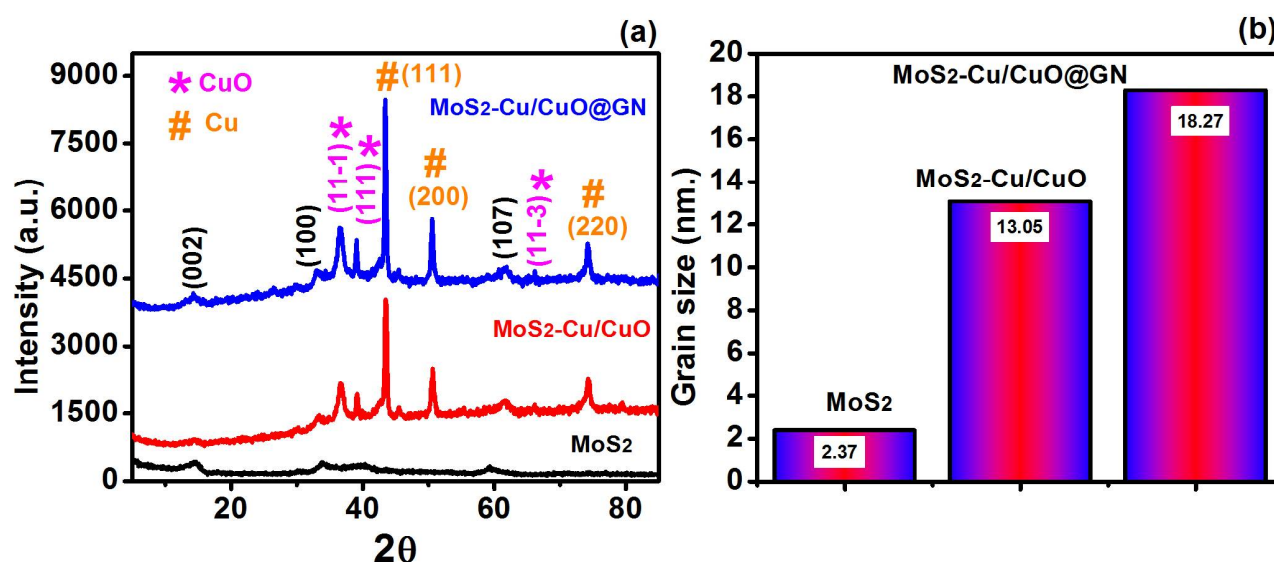
$$D = \frac{K\lambda}{\beta cos\theta} \tag{3}$$

Figure 1. Diffraction analysis (**a**) and grain size calculation (**b**) for MoS$_2$, MoS$_2$-Cu/CuO and MoS$_2$-Cu/CuO@GN.

Table 1. Calculated structural parameters for MoS$_2$, MoS$_2$-Cu/CuO and MoS$_2$-Cu/CuO@GN.

Material Details	Grain Size (nm)	Dislocation	Lattice Strain	Cell Volume Only for MoS$_2$
MoS$_2$	2.37	4.46×10^{-1}	2.01×10^{-2}	10.84
MoS$_2$-Cu/CuO	13.05	1.81×10^{-2}	4.00×10^{-3}	10.96
MoS$_2$-Cu/CuO@GN	18.27	1.96×10^{-2}	3.79×10^{-3}	10.47

The crystal grain size of MoS$_2$ was around 2.37 nm, while it was increased to 13.05 and 18.27, respectively, for MoS$_2$-Cu/CuO and MoS$_2$-Cu/CuO@GN. This increment in the crystal grain size has a direct relation to the enhancement of the photocatalytic activity of the material, as reported previously [28]. It could also be noticed that (Section 3.5) MoS$_2$-Cu/CuO@GN enhanced the photocatalytic activity in comparison to MoS$_2$ and

MoS$_2$-Cu/CuO. The interaction of Cu/CuO and GN can further lead to a change in the dislocation density of MoS$_2$ and be calculated by the following equation [29].

$$\delta = \frac{1}{D^2} \tag{4}$$

The dislocation density was calculated around 4.43×10^{-1}, 1.81×10^{-2} and 1.96×10^{-2}, respectively, for MoS$_2$, MoS$_2$-Cu/CuO and MoS$_2$-Cu/CuO@GN. This variation in the location density further leads to a change in the lattice strain of MoS$_2$ after the addition of Cu/CuO and GN. This change was calculated by the following relation [30].

$$\varepsilon = \frac{\beta cos\theta}{4} \tag{5}$$

The lattice strain was around 2.01×10^{-2}, 4.00×10^{-3} and 3.79×10^{-3}, respectively, for MoS$_2$, MoS$_2$-Cu/CuO and MoS$_2$-Cu/CuO@GN. In summary, the structural analysis (Table 1) showed the change in the lattice parameter of MoS$_2$ after the addition of Cu/CuO and GN. However, this addition does not lead to a change in the diffraction orientation or phase of MoS$_2$.

3.2. Optical Properties

The surface oxygen defects and charge recombination in the photocatalytic material can affect the catalytic efficiency which can be estimated by the PL spectra. Moreover, the peak intensity of PL spectra is attributed to the charge recombination during charge propagation from the valence to conduction band. The PL spectra (Figure 2a) of MoS$_2$, MoS$_2$-Cu/CuO and MoS$_2$-Cu/CuO@GN was recorded from 350 to 650 nm, having the 320 nm excitation wavelength. The PL intensity of the MoS$_2$ is higher in comparison to MoS$_2$-Cu/CuO and MoS$_2$-Cu/CuO@GN, which revealed the higher recombination rate of the charged carrier in MoS$_2$. However, the intensity of MoS$_2$ reduced after the addition of Cu/CuO (i.e., MoS$_2$-Cu/CuO), which indicated the role of Cu/CuO for charge separation and transfer at the heterojunction of MoS$_2$-Cu/CuO [31]. Moreover, the decrease in the PL intensity of MoS$_2$-Cu/CuO was also associated to the chemisorption absorption of the oxygen over the surface of the catalyst, which resulted in the enhanced charge separation [32]. PL intensity was further reduced for MoS$_2$-Cu/CuO@GN and this lessening is attributed to the interface between GN and MoS$_2$-Cu/CuO. Moreover, functional groups attached to the basal planes of GN provided the attractive site to enhance the charge carrier movement by reducing the charge recombination, which ultimately enhanced the catalytic activity of the MoS$_2$-Cu/CuO@GN [33].
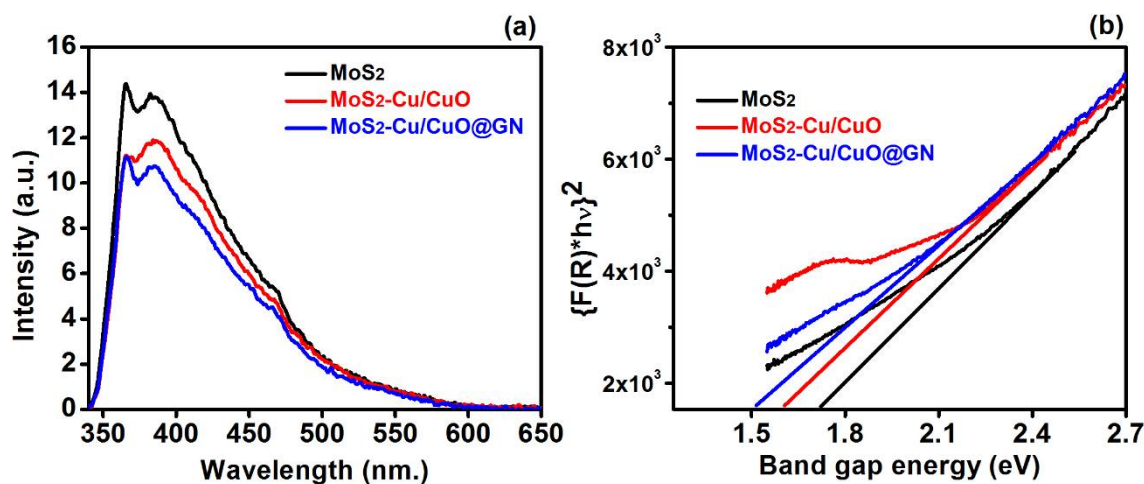

Figure 2. PL analysis (**a**) and band gap calculation (**b**) for MoS$_2$, MoS$_2$-Cu/CuO and MoS$_2$-Cu/CuO@GN.

The change in the recombination of the charge carrier can change the band gap of the MoS_2, which ultimately affects the photocatalytic activity. Therefore, the band gap of MoS_2, MoS_2-Cu/CuO and MoS_2-Cu/CuO@GN was estimated by applying the Kubelka–Munk relation [34]. The band gap of MoS_2 (Figure 2b) was approximately 1.7 eV which is consistent with the previous literature [35]. The band gap of MoS_2 reduced to 1.60 eV after the addition of Cu/CuO (MoS_2-Cu/CuO). This reduction in the band gap is attributed to the absorption ability of Cu/CuO in the visible region, which results in the reduction of the MoS_2-Cu/CuO band gap [36]. The band gap of MoS_2-Cu/CuO@GN was approximately 1.50 eV, which enlightens the role of GN to reduce the band gap. Generally, the GN has an sp2 band and other oxygen functional groups in the form of epoxy (C-O-C) and hydroxyl (OH) which enhances the charge carrier mobility with the absorption of light in the GN-based composites [37].

3.3. Surface Compositional Analysis

The compositional analysis of MoS_2, MoS_2-Cu/CuO and MoS_2-Cu/CuO@GN was acquired by the XPS survey scan. The surface composition (Figure 3a) of MoS_2 revealed the presence of Mo3d, O1s and S2p with the atomic percentage of approximately 25.5%, 30.6 and 43.9%, respectively. There was no other element observed which shows the accuracy of the synthesis approach and is also consistent with our XRD diffraction pattern. The survey spectra of MoS_2-Cu/CuO revealed the appearance of Cu2p3 in addition to Mo3d, O1s and S2p. Moreover, the incorporation of GN was confirmed by the presence of the C1s peak in MoS_2-Cu/CuO@GN and was approximately 46.7%. Table 2 shows the detected atomic percentage of each detected element in the prepared catalyst.
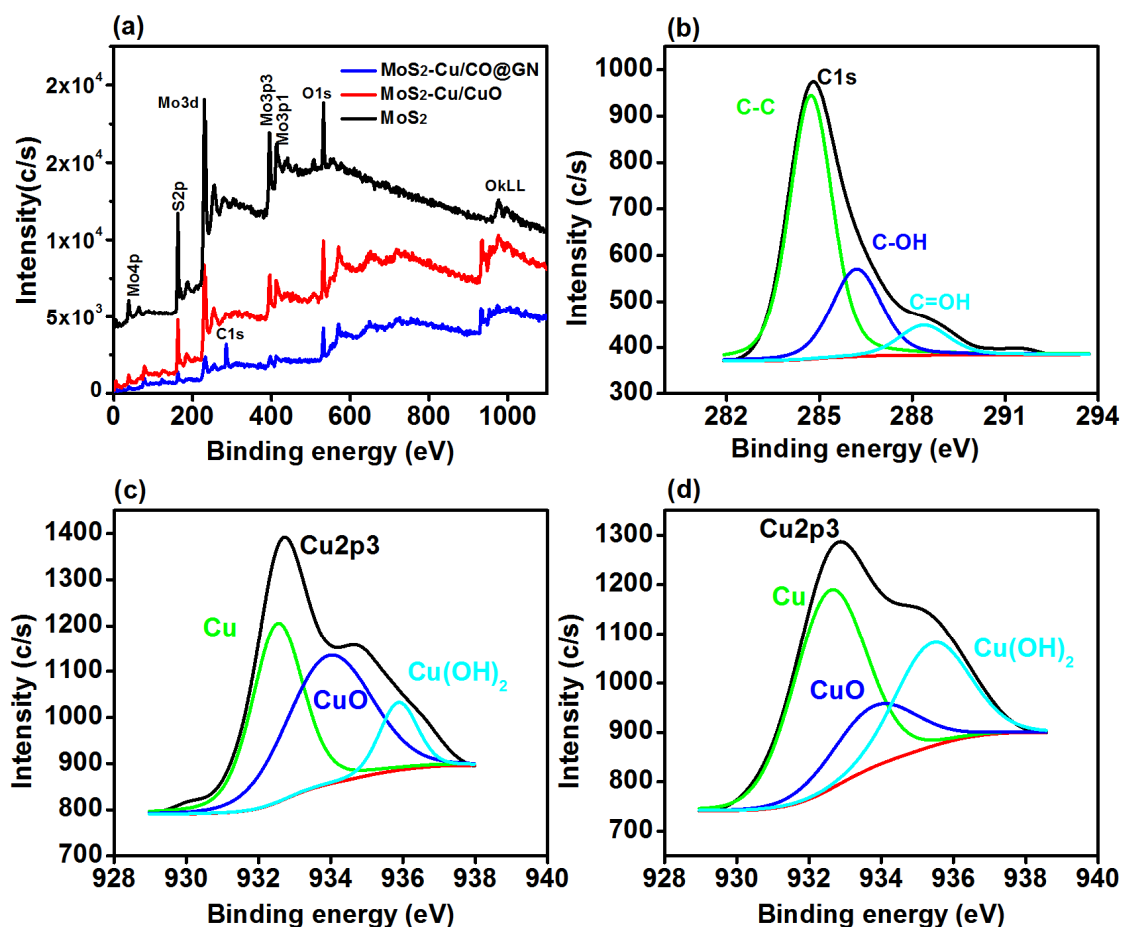

Figure 3. (**a**) Survey scan for MoS_2, MoS_2-Cu/CuO and MoS_2-Cu/CuO@GN, (**b**) high resolution C1s spectra of MoS_2-Cu/CuO@GN and (**c**,**d**) high resolution Cup2 analysis for MoS_2-Cu/CuO and MoS_2-Cu/CuO@GN.

Table 2. XPS Elemental composition of MoS$_2$, MoS$_2$-Cu/CuO and MoS$_2$-Cu/CuO@GN.

Sample Detail	Detected Element (%)				
	S2p	O1s	Mo3d	Cu2P3	C1s
MoS$_2$	43.9	30.6	25.5	—	—–
MoS$_2$ Cu/CuO	30.5	42.1	18.4	8.9	—–
MoS$_2$ Cu/CuO@GN	10.6	28.9	6.0	7.8	46.7

The C1s spectra (Figure 3b) of MoS$_2$-Cu/CuO@GN revealed the presence of three peaks approximately at 284.73 eV, 286.06 and 288.34 eV and attributed, respectively, to the C-C (65.82%), C-OH (25.44%) and C=O (8.74%) functional groups [38,39]. These functional groups of GN are important to facilitate/capture the dye molecules which, as a result, enhanced the catalytic activity of MoS$_2$-Cu/CuO@GN [16].

Cu2p3 of MoS$_2$-Cu/CuO (Figure 3c) revealed three peaks at 532.7 eV, 533.5 and 935.4 eV which are attributed to Cu, CuO and Cu (OH)$_2$ [40,41]. Cu was approximately 53.13%, while CuO and Cu (OH)$_2$ were, respectively, 18.70 and 28.17%. However, after the induction of GN (Figure 3d), the contribution of Cu changed from 53.13 to 42.41%, while CuO increased from 18.76 to 46.22%. In conclusion, the Cu2p3 analysis of MoS$_2$-Cu/CuO and MoS$_2$-Cu/CuO@GN confirms the presence of a mixed phase of Cu/CuO and is consistent with our XRD findings.

High-resolution spectra of Mo3d (Figure 4) show the four peaks which confirm the interaction of molybdenum with oxygen and sulfur. The MoS$_2$ (Figure 4a) have peaks around 229.0 eV, 229.3, 232.5 and 232.8 eV which are, respectively, attributed to Mo, MoS$_2$, MoS$_3$ and MoO$_3$ [41,42]. However, the Mo, MoS$_2$, MoS$_3$ and MoO$_3$ contribution was changed with the addition of Cu/CuO and GN, as revealed in (Figure 4b–d). This change in the metal and oxide interaction can lead to changes in the photocatalytic activity of the catalyst [43].
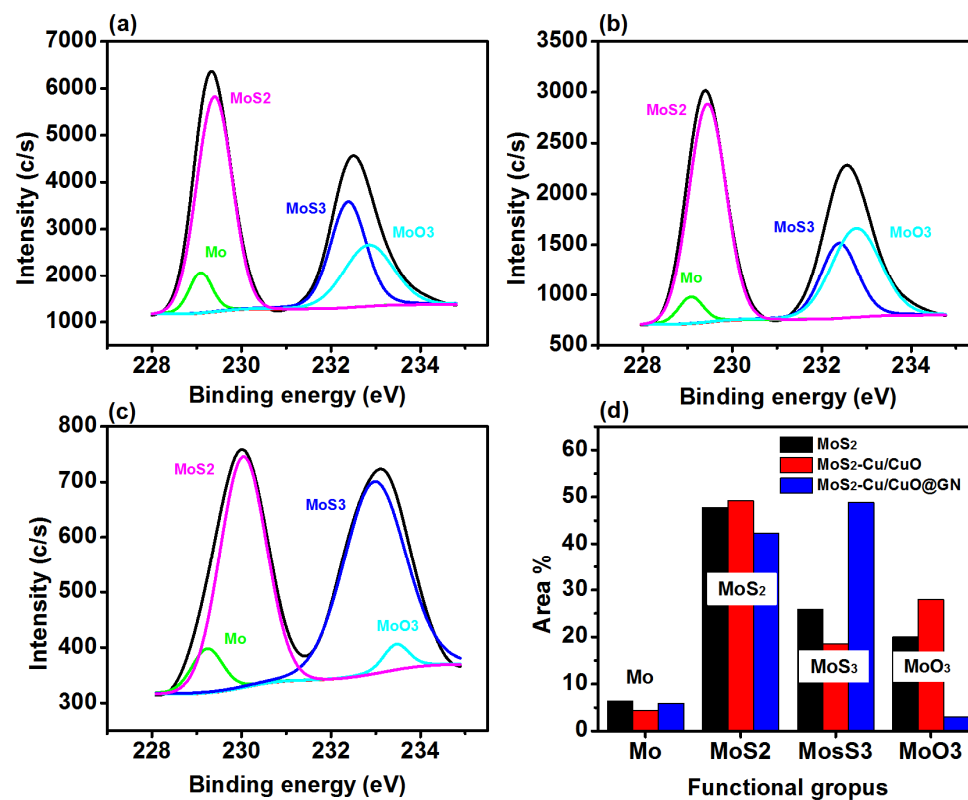
Figure 4. Mo3d spectra (**a**) MoS2, (**b**) MoS$_2$-Cu/CuO, (**c**) MoS$_2$-Cu/CuO@GN and (**d**) functional groups for MoS$_2$, MoS$_2$-Cu/CuO and MoS$_2$-Cu/CuO@GN.

O1s spectra of MoS_2 (Figure 5a) revealed the appearance of two peaks at approximately 530.9 and 532.5 eV which are attributed to the oxidation of O1s (O^-) and OH [41,44]. However, the small shift in the contribution of O^- (87.08 to 87.55%) and OH (12.92 to 12.45%) were seen in the Cu/CuO counterpart (Figure 5b), which could be due to possible interactions among the constituent elements. The addition of GN to MoS_2-Cu/CuO resulted in an additional peak (Figure 5c) at approximately 529.02 eV which presents the C–O bonding with the contribution of 15.41% [41].
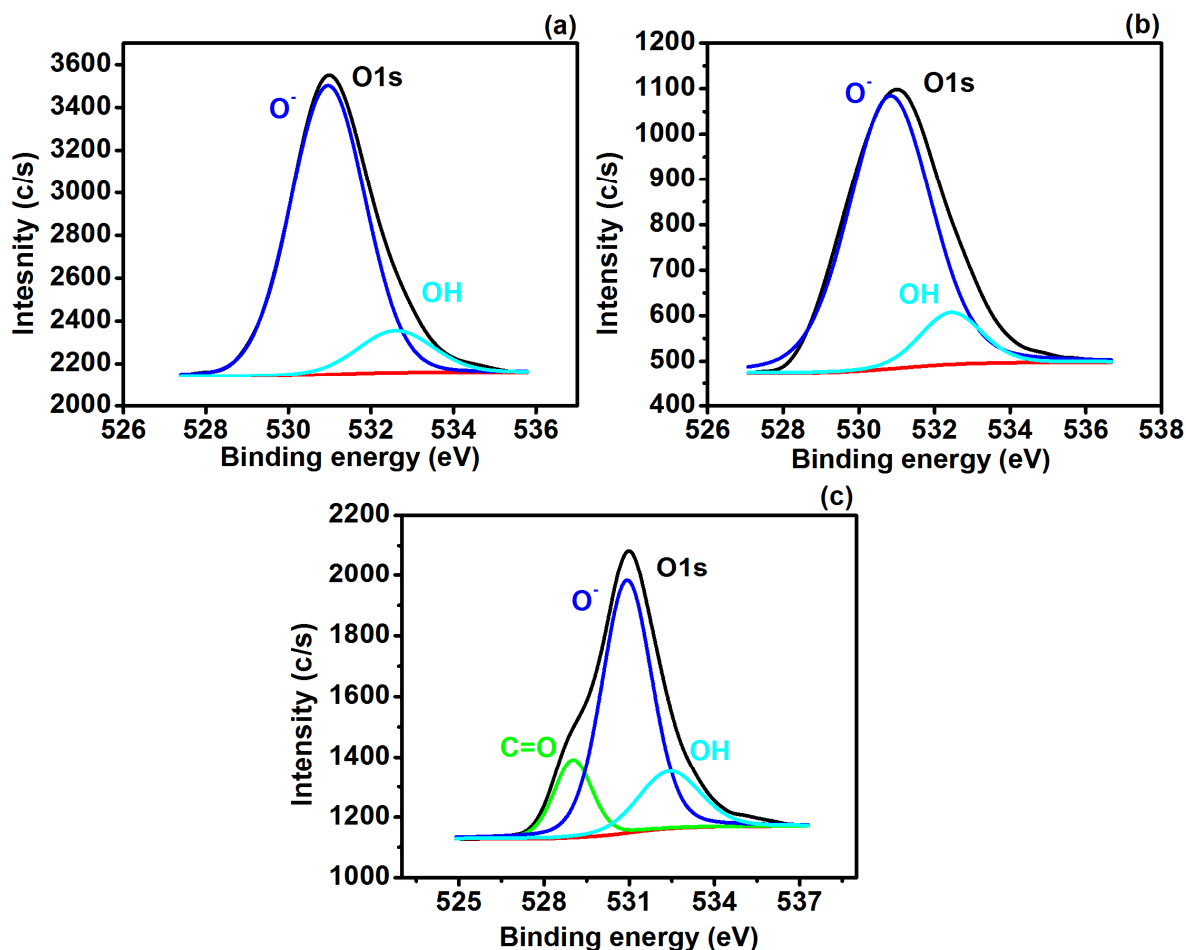

Figure 5. High-resolution O1s analysis for (**a**) MoS_2, (**b**) MoS_2-Cu/CuO and (**c**) MoS_2-Cu/CuO@GN.

3.4. Surface Morphology

FESEM images of MoS_2 (Figure 6a) shows the stacked petal-like structure of MoS_2 which is also consistent with previous reports [45]. The surface morphology of MoS_2-Cu/CuO (Figure 6b) shows the appearance of some clusters of nanoparticles in addition to the stacked petal-like structure of MoS_2 which are the Cu/CuO nanoparticles. Further, with the addition of GN (Figure 6c), flakes were observed with clustered MoS_2 which is due to the possible interactions of GN with MoS_2 and Cu/CuO [46].

3.5. Photocatalytic Activity

The photocatalytic activity of the prepared MoS_2, MoS_2-Cu/CuO and MoS_2-Cu/CuO@GN was tested against the degradation of MB. The UV abortion peak of MB appeared at 665 nm and was monitored for the purpose of degradation. Figure 7a–c show the time-dependent dilapidation of the MB characteristic peak in the presence of MoS_2, MoS_2-Cu/CuO and MoS_2-Cu/CuO@GN, respectively. The intensity in Figure 7c was found lower in comparison to Figure 7a,b under the same experimental conditions, having the same concentration of MB. This lower intensity revealed a faster degradation rate. Figure 7d,e

show the degradation percentage rate of MB within the 30 min for MoS_2, MoS_2-Cu/CuO and MoS_2-Cu/CuO@GN. MoS_2 and Cu/CuO degraded the MB around 77.8% and 20.4%, respectively, within 30 min under the visible light irradiation. However, the degradation ability of MoS_2 accelerated after the addition of Cu/CuO and GN. Therefore, the degradation of MoS_2-Cu/CuO and MoS_2-Cu/CuO@GN was found to be 86.6 and 93.8%, respectively. The enhanced degradation ability of MoS_2-Cu/CuO in comparison to MoS_2 revealed the role of Cu/CuO to enhance the photocatalytic activity. This enhanced photocatalytic performance of MoS_2-Cu/CuO attributed to the formation of a heterojunction, which ultimately enhanced the charge separation and slowed down the charge recombination ratio [47]. The photocatalytic activity of MoS_2-Cu/CuO enhanced after the addition of GN. Therefore, MoS_2-Cu/CuO@GN has a 93.8% efficiency for the degradation of MB within 30 min. This enhanced photocatalytic activity is also attributed to the surface area of the catalyst. The surface area of the MoS_2 was found to be around 280.45 m^2/g, while the surface area of MoS_2-Cu/CuO and MoS_2-Cu/CuO@GN was, respectively, 285.20 and 297.50 m^2/g (Figure S2). This enhanced surface area also provides an ample active site to capture the dye molecules. Moreover, GN provided the support in electron transport and lessened the recombination of the charge carried, which resulted in the enhancement of the catalytic activity of MoS_2-Cu/CuO@GN [48]. This change in the movement of the charge particle may affect the reaction rate constant (k) which is shown in Figure 7f. The order of the reaction rate constant was MoS_2-Cu/CuO@GN > MoS_2-Cu/CuO > MoS_2 with values, respectively, of 5.01×10^{-2}, 6.69×10^{-2} and 9.26×10^{-2}.
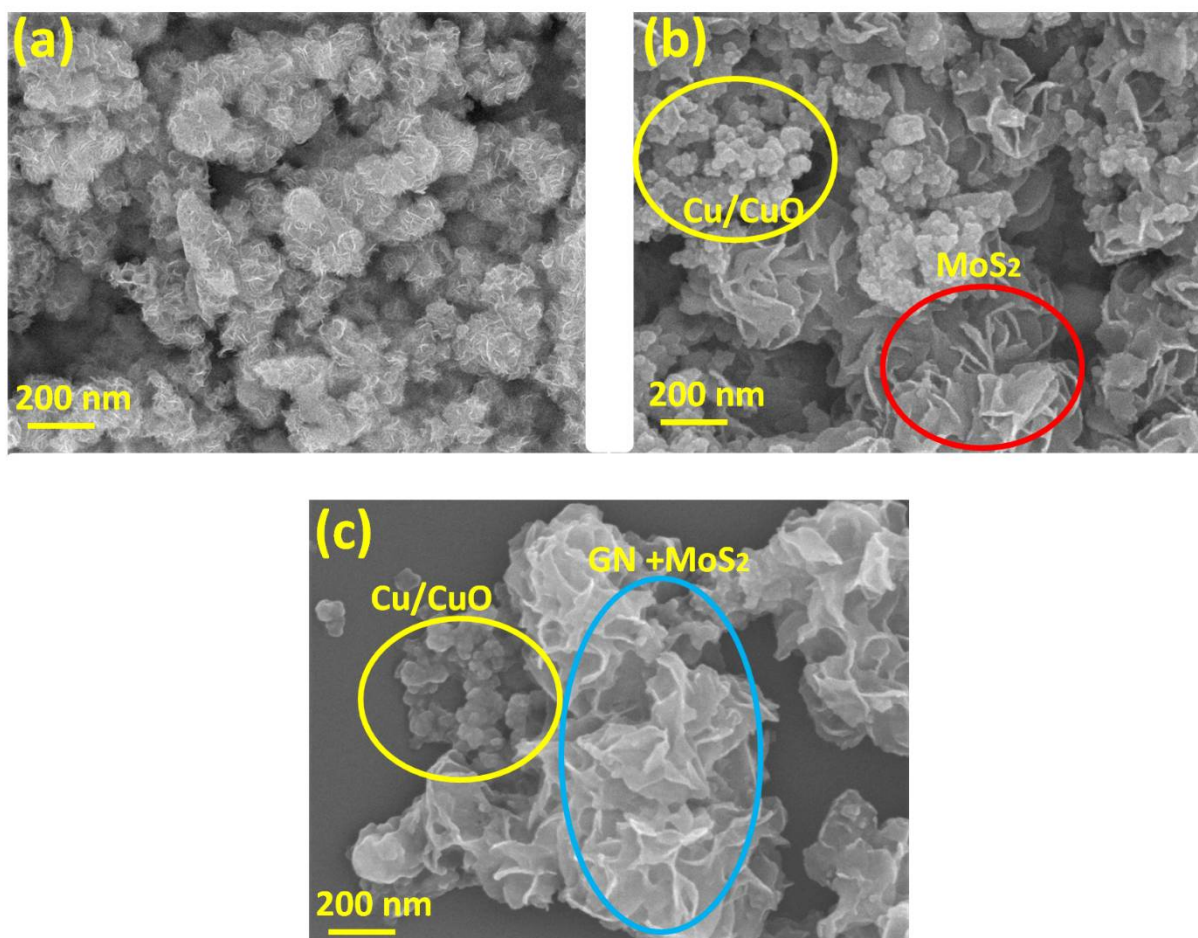
Figure 6. Surface morphology of (**a**) MoS_2, (**b**) MoS_2-Cu/CuO and (**c**) MoS_2-Cu/CuO@GN.
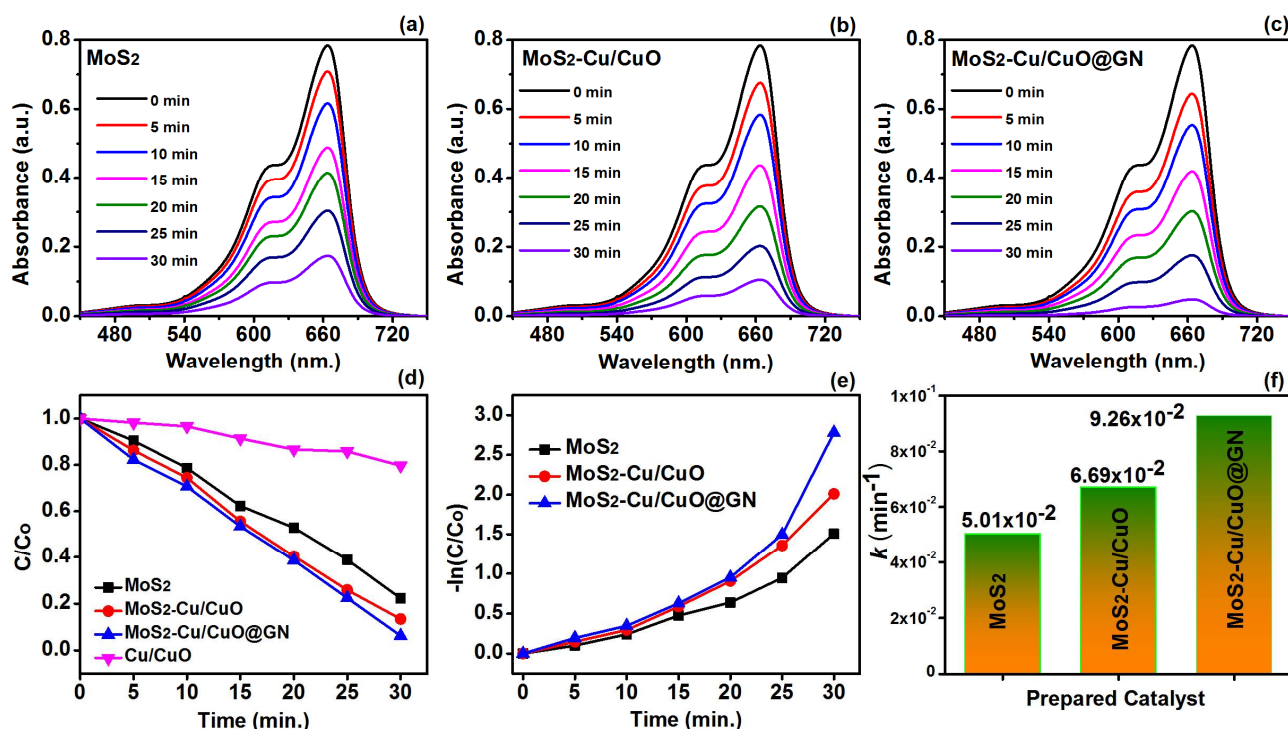
Figure 7. (**a**–**c**) Time-dependent dilapidation of the MB characteristic peak in the presence of Cu/CuO, MoS$_2$, MoS$_2$-Cu/CuO and MoS$_2$-Cu/CuO@GN, (**d**,**e**) degradation percentage rate of MB within 30 min and (**f**) reaction rate constant of MoS$_2$, MoS$_2$-Cu/CuO and MoS$_2$-Cu/CuO@GN.

3.5.1. Effect of Reaction Parameter

Effect of MoS$_2$-Cu/CuO@GN Dosage

The degradation of MB can further be associated with the dosage concentration of MoS$_2$-Cu/CuO@GN. The concentration of the catalyst played a vital role in producing the active site which assisted the degradation of the pollutant. However, an excess of active sites can render the catalytic performance. In this regard, the concentration of MoS$_2$-Cu/CuO@GN was chosen from 15 to 35 mg, having an interval of 5 mg. The degradation efficiency was 76.69% at 15 mg/200 mL which further increased to 78.79 and 93.80, respectively, for 20 and 25 mg/200 mL, as shown in Figure 8a–c. This increasing trend in the degradation efficiency of MB with the increase in the MoS$_2$-Cu/CuO@GN dosage revealed the ample active site on the surface of the prepared catalysts to capture and degrade the dye molecules. However, the catalytic efficiency was reduced to 88.17 (30 mg/200 mL) and 85.82% (35 mg/200 mL) with a further increase to the MoS$_2$-Cu/CuO@GN dosage. This indicates that the blocking of the active sight and scattering of light radiation also affects the reaction rate constant (k) during the photocatalytic process.

Effect of Hydrogen Peroxide

The catalytic properties of the material can be tuned by adjusting the reaction parameters, such as by introducing the scavenging of free radicals. In this regard, H$_2$O$_2$ is commonly used for the production of reactive oxygen species such as hydroxyl radicals and superoxide during the photocatalytic reaction. These generated radicals can react with MB to enhance the photocatalytic efficiency. Therefore, we decided to investigate the photocatalytic activity of MoS$_2$-Cu/CuO@GN at different concentrations of H$_2$O$_2$, i.e., 0, 2, 4, 6 and 8 mL. Figure 8d–f show the change in the reaction kinetics of MoS$_2$-Cu/CuO@GN with the addition of H$_2$O$_2$. The degradation efficiency of MoS$_2$-Cu/CuO@GN was approximately 93.8% in the absence of H$_2$O$_2$, having a rate constant of 0.092.min^{-1}. However, the efficiency increased to 98.5% at 4% of H$_2$O$_2$, with the highest rate constant of 0.141 min^{-1}. This revealed the generation of maximum free radicals that interacts with MB during the

degradation process. However, the catalytic efficiency of MoS$_2$-Cu/CuO@GN was reduced to 96.5% and 93.1 %, respectively, for 6 and 8mL of H$_2$O$_2$. This showed that free radicals react with H$_2$O$_2$ rather than MB which ultimately reduced the photocatalytic efficiency [49].
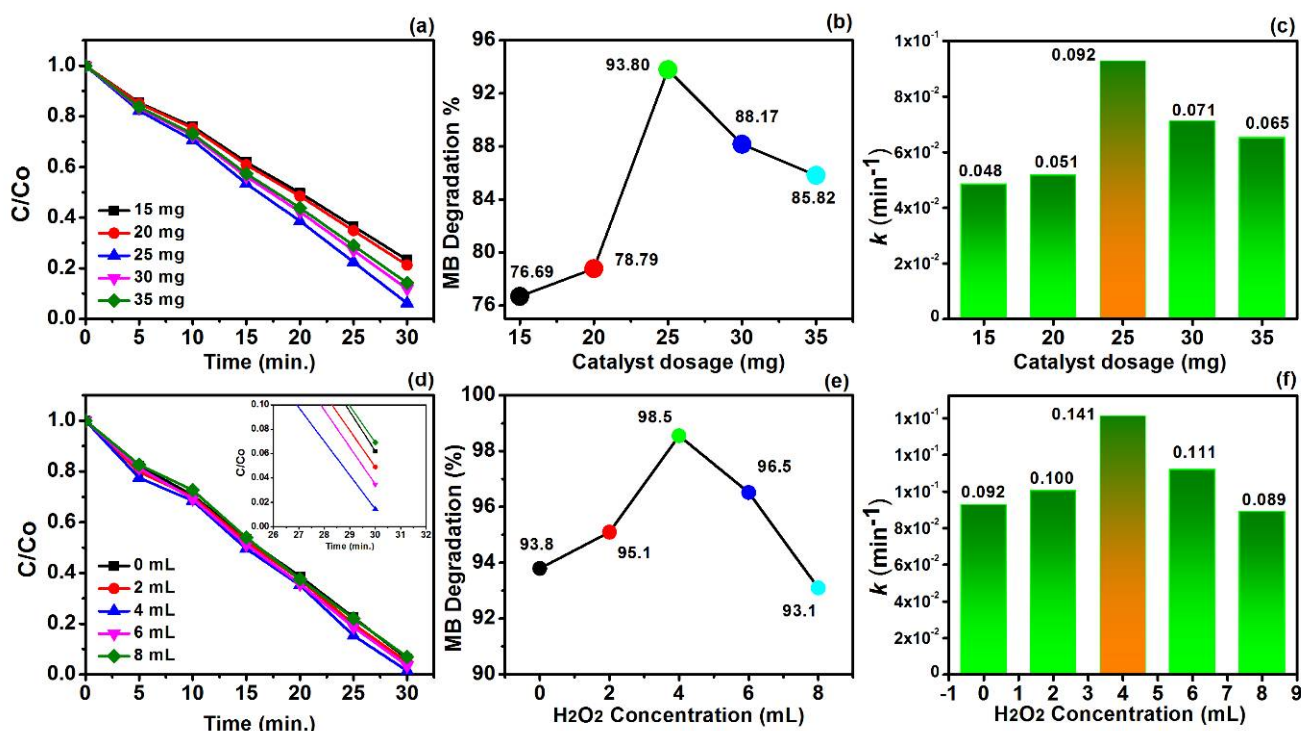

Figure 8. (**a**–**c**) Change in the reaction kinetics at different dosages of MoS$_2$-Cu/CuO@GN, (**d**–**f**) change in the reaction kinetics at different dosages of hydrogen peroxide.

Reusability of MoS$_2$-Cu/CuO@GN

The reusability of the photocatalysts matters for their potential application. Therefore, the cyclic reusability of MoS$_2$-Cu/CuO@GN was tested. The five consecutive cyclic photocatalytic experiments were performed. A total of 25 mg of MoS$_2$-Cu/CuO@GN was added to 20 ppm of MB solution having 4% of H$_2$O$_2$. The sample was separated through a centrifuge (3000 rpm/min) after completing each cycle. The cyclic results (Figure 9) revealed that the photocatalytic efficiency remained at 96.3% after five consecutive cycles under the same experimental conditions.
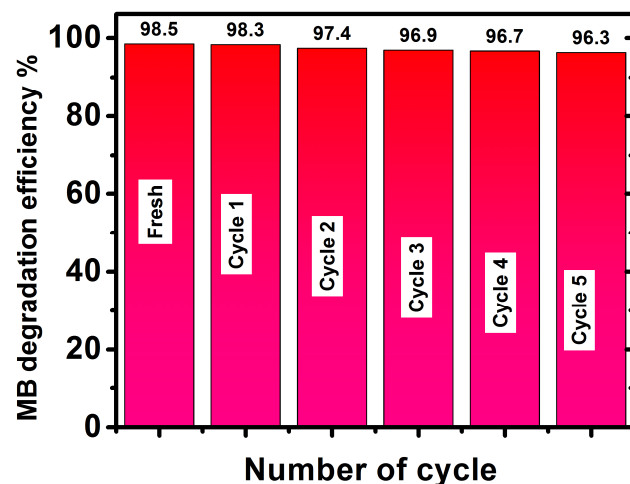

Figure 9. Reusability of MoS$_2$-Cu/CuO@GN photocatalysts under same experimental conditions.

4. Conclusions

In conclusion, the addition of Cu/CuO and GN accelerated the photocatalytic activity of MoS_2 under certain optimized experimental conditions. This enhanced the photocatalytic activity of MoS_2-Cu/CuO@GN, attributed to the change in the charge carrier movement, the alteration in the recombination ratio, the band gap, the interaction of the present element and the structural properties. The band gap of MoS_2 reduced to 1.5 eV from 1.7 eV. Moreover, Cu/CuO and GN supports the chemisorption absorption of the oxygen over the surface of the catalyst by providing the more active sites, which resulted in the enhanced photocatalytic activity. The structural analysis revealed the increase in the grain size of MoS_2 (2.37 nm) with the addition of Cu/CuO (13.05 nm) and GN (18.27 nm) without changing the preferred crystal orientation. The XPS analysis confirms the variation in the C-C, C-OH, C=O and OH functional groups of MoS_2 with the addition of Cu/CuO and GN, which is attributed to the enhanced photocatalytic activity. In short, this study revealed the potential use of polymer-based nanocomposites with metal, metal oxides and graphene for wastewater treatment through a facile photocatalytic process.

Supplementary Materials: The following supporting information can be downloaded at: https://www.mdpi.com/article/10.3390/polym14163259/s1, Figure S1. (a) Degradation of MB under the different concentration MoS_2 (b) Degradation of optimized 25 mg of MoS_2 at various pH within the 30 minutes. Figure S2. BET specific surface area of MoS_2, MoS_2-Cu/CuO MoS_2-Cu/CuO @GN.

Author Contributions: Conceptualization A.J.; Methodology A.J. and A.A.M.; Formal analysis A.J.; Writing—original draft A.J.; Funding acquisition A.J; Writing—review editing A.J. and A.A.M. All authors have read and agreed to the published version of the manuscript.

Institutional Review Board Statement: Not Applicable.

Informed Consent Statement: Not Applicable.

Data Availability Statement: Data will be available on request.

Conflicts of Interest: The authors declare no conflict of interest.

References

1. Chakraborty, J.; Nath, I.; Verpoort, F. A physicochemical introspection of porous organic polymer photocatalysts for wastewater treatment. *Chem. Soc. Rev.* **2022**, *51*, 1124–1138. [CrossRef] [PubMed]
2. Zhang, S.; Guo, S.; Li, A.; Liu, D.; Sun, H.; Zhao, F. Low-cost bauxite residue-MoS2 possessing adsorption and photocatalysis ability for removing organic pollutants in wastewater. *Sep. Purif. Technol.* **2022**, *283*, 120144. [CrossRef]
3. Chai, W.S.; Cheun, J.Y.; Kumar, P.S.; Mubashir, M.; Majeed, Z.; Banat, F.; Ho, S.-H.; Show, P.L. A review on conventional and novel materials towards heavy metal adsorption in wastewater treatment application. *J. Clean. Prod.* **2021**, *296*, 126589. [CrossRef]
4. Mohana Roopan, S.; Khan, M.A. MoS2 based ternary composites: Review on heterogeneous materials as catalyst for photocatalytic degradation. *Catal. Rev.* **2021**, 1–74. [CrossRef]
5. Gautam, S.; Agrawal, H.; Thakur, M.; Akbari, A.; Sharda, H.; Kaur, R.; Amini, M. Metal oxides and metal organic frameworks for the photocatalytic degradation: A review. *J. Environ. Chem. Eng.* **2020**, *8*, 103726. [CrossRef]
6. Heuer, J.; Ferguson, C.T.J. Photocatalytic polymer nanomaterials for the production of high value compounds. *Nanoscale* **2022**, *14*, 1646–1652. [CrossRef]
7. Kim, A.R.; Vinothkannan, M.; Ramakrishnan, S.; Park, B.-H.; Han, M.-K.; Yoo, D.J. Enhanced electrochemical performance and long-term durability of composite membranes through a binary interface with sulfonated unzipped graphite nanofibers for polymer electrolyte fuel cells operating under low relative humidity. *Appl. Surf. Sci.* **2022**, *593*, 153407. [CrossRef]
8. Rani, A.; Singh, K.; Sharma, P. Investigation of visible light photocatalytic degradation of organic dyes by MoS2 nanosheets synthesized by different routes. *Bull. Mater. Sci.* **2022**, *45*, 63. [CrossRef]

9.   Lai, M.T.L.; Lee, K.M.; Yang, T.C.K.; Pan, G.T.; Lai, C.W.; Chen, C.-Y.; Johan, M.R.; Juan, J.C. The improved photocatalytic activity of highly expanded MoS2 under visible light emitting diodes. *Nanoscale Adv.* **2021**, *3*, 1106–1120. [CrossRef]

10. Hegazy, M.A.; Ezzat, H.A.; Yahia, I.S.; Zahran, H.Y.; Elhaes, H.; Gomaa, I.; Ibrahim, M.A. Effect of CuO and Graphene on PTFE Microfibers: Experimental and Modeling Approaches. *Polymers* **2022**, *14*, 1069. [CrossRef]

11. Xu, H.; Zhu, J.; Ma, Q.; Ma, J.; Bai, H.; Chen, L.; Mu, S. Two-Dimensional MoS_2: Structural Properties, Synthesis Methods, and Regulation Strategies toward Oxygen Reduction. *Micromachines* **2021**, *12*, 240. [CrossRef]

12. Li, H.; Yu, K.; Lei, X.; Guo, B.; Li, C.; Fu, H.; Zhu, Z. Synthesis of the MoS_2@CuO heterogeneous structure with improved photocatalysis performance and H_2O adsorption analysis. *Dalton Trans.* **2015**, *44*, 10438–10447. [CrossRef]

13. Ashar, A.; Bhatti, I.A.; Jilani, A.; Mohsin, M.; Rasul, S.; Iqbal, J.; Shakoor, M.B.; Al-Sehemi, A.G.; Wageh, S.; Al-Ghamdi, A.A. Enhanced Solar Photocatalytic Reduction of Cr(VI) Using a (ZnO/CuO) Nanocomposite Grafted onto a Polyester Membrane for Wastewater Treatment. *Polymers* **2021**, *13*, 4047. [CrossRef]

14. Xu, L.; Srinivasakannan, C.; Peng, J.; Zhang, L.; Zhang, D. Synthesis of Cu-CuO nanocomposite in microreactor and its application to photocatalytic degradation. *J. Alloys Compd.* **2017**, *695*, 263–269. [CrossRef]

15. Jinfeng, Z.; Yunguang, Y.; Wei, L. Preparation, Characterization, and Activity Evaluation of CuO/F-TiO_2 Photocatalyst. *Int. J. Photoenergy* **2012**, *2012*, 139739. [CrossRef]

16. Jilani, A.; Othman, M.H.D.; Ansari, M.O.; Hussain, S.Z.; Ismail, A.F.; Khan, I.U.; Inamuddin. Graphene and its derivatives: Synthesis, modifications, and applications in wastewater treatment. *Environ. Chem. Lett.* **2018**, *16*, 1301–1323. [CrossRef]

17. Albero, J.; Mateo, D.; García, H. Graphene-Based Materials as Efficient Photocatalysts for Water Splitting. *Molecules* **2019**, *24*, 906. [CrossRef]

18. Saeed, U.; Jilani, A.; Iqbal, J.; Al-Turaif, H. Reduced graphene oxide-assisted graphitic carbon nitride@ZnO rods for enhanced physical and photocatalytic degradation. *Inorg. Chem. Commun.* **2022**, *142*, 109623. [CrossRef]

19. Gusain, R.; Kumar, N.; Opoku, F.; Govender, P.P.; Ray, S.S. MoS_2 Nanosheet/ZnS Composites for the Visible-Light-Assisted Photocatalytic Degradation of Oxytetracycline. *ACS Appl. Nano Mater.* **2021**, *4*, 4721–4734. [CrossRef]

20. Trang Phan, T.T.; Truong, T.T.; Huu, H.T.; Nguyen, L.T.; Nguyen, V.T.; Nguyen, H.L.; Vo, V. Visible Light-Driven Mn-MoS_2/rGO Composite Photocatalysts for the Photocatalytic Degradation of Rhodamine B. *J. Chem.* **2020**, *2020*, 6285484. [CrossRef]

21. Jilani, A.; Othman, M.H.D.; Ansari, M.O.; Kumar, R.; Alshahrie, A.; Ismail, A.F.; Khan, I.U.; Sajith, V.K.; Barakat, M.A. Facile spectroscopic approach to obtain the optoelectronic properties of few-layered graphene oxide thin films and their role in photocatalysis. *New J. Chem.* **2017**, *41*, 14217–14227. [CrossRef]

22. Khan, A.; Rashid, A.; Younas, R.; Chong, R. A chemical reduction approach to the synthesis of copper nanoparticles. *Int. Nano Lett.* **2016**, *6*, 21–26. [CrossRef]

23. Dustgeer, M.R.; Asma, S.T.; Jilani, A.; Raza, K.; Hussain, S.Z.; Shakoor, M.B.; Iqbal, J.; Abdel-wahab, M.S.; Darwesh, R. Synthesis and characterization of a novel single-phase sputtered Cu_2O thin films: Structural, antibacterial activity and photocatalytic degradation of methylene blue. *Inorg. Chem. Commun.* **2021**, *128*, 108606. [CrossRef]

24. Mudassir, M.A.; Hussain, S.Z.; Jilani, A.; Zhang, H.; Ansari, T.M.; Hussain, I. Magnetic Hierarchically Macroporous Emulsion-Templated Poly(acrylic acid)–Iron Oxide Nanocomposite Beads for Water Remediation. *Langmuir* **2019**, *35*, 8996–9003. [CrossRef]

25. Mishra, S.K.; Tripathi, S.N.; Choudhary, V.; Gupta, B.D. SPR based fibre optic ammonia gas sensor utilizing nanocomposite film of PMMA/reduced graphene oxide prepared by in situ polymerization. *Sens. Actuators B Chem.* **2014**, *199*, 190–200. [CrossRef]

26. Gascho, J.L.S.; Costa, S.F.; Recco, A.A.C.; Pezzin, S.H. Graphene Oxide Films Obtained by Vacuum Filtration: X-ray Diffraction Evidence of Crystalline Reorganization. *J. Nanomater.* **2019**, *2019*, 5963148. [CrossRef]

27. Jilani, A.; Hussain, S.Z.; Melaibari, A.A.; Abu-Hamdeh, N.H. Development and Mechanistic Studies of Ternary Nanocomposites for Hydrogen Production from Water Splitting to Yield Sustainable/Green Energy and Environmental Remediation. *Polymers* **2022**, *14*, 1290. [CrossRef]

28. Nandiyanto, A.B.D.; Zaen, R.; Oktiani, R. Correlation between crystallite size and photocatalytic performance of micrometer-sized monoclinic WO3 particles. *Arab. J. Chem.* **2020**, *13*, 1283–1296. [CrossRef]

29. Jilani, A.; Abdel-wahab, M.S.; Al-ghamdi, A.A.; Dahlan, A.s.; Yahia, I.S. Nonlinear optical parameters of nanocrystalline AZO thin film measured at different substrate temperatures. *Phys. B Condens. Matter* **2016**, *481*, 97–103. [CrossRef]

30. Jilani, A.; Othman, M.H.D.; Ansari, M.O.; Oves, M.; Alshahrie, A.; Khan, I.U.; Sajith, V. A simple route to layer-by-layer assembled few layered graphene oxide nanosheets: Optical, dielectric and antibacterial aspects. *J. Mol. Liq.* **2018**, *253*, 284–296. [CrossRef]

31. Jeong, D.; Jo, W.; Jeong, J.; Kim, T.; Han, S.; Son, M.-K.; Jung, H. Characterization of Cu_2O/CuO heterostructure photocathode by tailoring CuO thickness for photoelectrochemical water splitting. *RSC Advances* **2022**, *12*, 2632–2640. [CrossRef]

32. Gopal, R.; Chinnapan, M.M.; Bojarajan, A.K.; Rotte, N.K.; Ponraj, J.S.; Ganesan, R.; Atanas, I.; Nadarajah, M.; Manavalan, R.K.; Gaspar, J. Facile synthesis and defect optimization of 2D-layered MoS_2 on TiO_2 heterostructure for industrial effluent, wastewater treatments. *Sci. Rep.* **2020**, *10*, 21625. [CrossRef]

33. Mondal, A.; Prabhakaran, A.; Gupta, S.; Subramanian, V.R. Boosting Photocatalytic Activity Using Reduced Graphene Oxide (RGO)/Semiconductor Nanocomposites: Issues and Future Scope. *ACS Omega* **2021**, *6*, 8734–8743. [CrossRef]

34. Jilani, A.; Othman, M.H.D.; Ansari, M.O.; Oves, M.; Hussain, S.Z.; Khan, I.U.; Abdel-wahab, M.S. Structural and optical characteristics, and bacterial decolonization studies on non-reactive RF sputtered Cu–ZnO@graphene based nanoparticles thin films. *J. Mater. Sci.* **2019**, *54*, 6515–6529. [CrossRef]

35. Wang, B.; Yang, S.; Chen, J.; Mann, C.; Bushmaker, A.; Cronin, S.B. Radiation-induced direct bandgap transition in few-layer MoS$_2$. *Appl. Phys. Lett.* **2017**, *111*, 131101. [CrossRef]

36. Singh, R.; Jit, S.; Tripathi, S. MoS$_2$, rGO, and CuO Nanocomposite-Based High Performance UV-Visible Dual-Band Photodetectors. *IEEE Photonics Technol. Lett.* **2021**, *33*, 93–96. [CrossRef]

37. Abid; Sehrawat, P.; Islam, S.S.; Mishra, P.; Ahmad, S. Reduced graphene oxide (rGO) based wideband optical sensor and the role of Temperature, Defect States and Quantum Efficiency. *Sci. Rep.* **2018**, *8*, 3537. [CrossRef]

38. Yan, S.; Yang, S.; He, L.; Ye, C.; Song, X.; Liao, F. Quantum size effect of poly(o-phenylenediamine) quantum dots: From controllable fabrication to tunable photoluminescence properties. *Synth. Met.* **2014**, *198*, 142–149. [CrossRef]

39. Muralikrishna, S.; Sureshkumar, K.; Varley, T.S.; Nagaraju, D.H.; Ramakrishnappa, T. In situ reduction and functionalization of graphene oxide with l-cysteine for simultaneous electrochemical determination of cadmium(ii), lead(ii), copper(ii), and mercury(ii) ions. *Anal. Methods* **2014**, *6*, 8698–8705. [CrossRef]

40. Zhang, T.; He, Y.; Wang, F.; Li, H.; Duan, C.; Wu, C. Surface analysis of cobalt-enriched crushed products of spent lithium-ion batteries by X-ray photoelectron spectroscopy. *Sep. Purif. Technol.* **2014**, *138*, 21–27. [CrossRef]

41. Moulder, J.F.; Chastain, J. *Handbook of X-ray Photoelectron Spectroscopy: A Reference Book of Standard Spectra for Identification and Interpretation of XPS Data*; Physical Electronics Division, Perkin-Elmer Corporation: Chanhassen, MN, USA, 1992.

42. Cheng, C.-K.; Lin, C.-H.; Wu, H.-C.; Ma, C.-C.M.; Yeh, T.-K.; Chou, H.-Y.; Tsai, C.-H.; Hsieh, C.-K. The Two-Dimensional Nanocomposite of Molybdenum Disulfide and Nitrogen-Doped Graphene Oxide for Efficient Counter Electrode of Dye-Sensitized Solar Cells. *Nanoscale Res. Lett.* **2016**, *11*, 117. [CrossRef] [PubMed]

43. Sinirtaş Ilkme, E.; Pozan Soylu, G.S. The role of some metal ions in enhancement of photocatalytic activity of Fe(2)O(3)-V(2)O(5) binary oxide. *Turk. J. Chem.* **2021**, *45*, 348–361. [CrossRef]

44. Giubileo, F.; Grillo, A.; Passacantando, M.; Urban, F.; Iemmo, L.; Luongo, G.; Pelella, A.; Loveridge, M.; Lozzi, L.; Di Bartolomeo, A. Field Emission Characterization of MoS2 Nanoflowers. *Nanomaterials* **2019**, *9*, 717. [CrossRef] [PubMed]

45. Zeng, X.; Niu, L.; Song, L.; Wang, X.; Shi, X.; Yan, J. Effect of Polymer Addition on the Structure and Hydrogen Evolution Reaction Property of Nanoflower-Like Molybdenum Disulfide. *Metals* **2015**, *5*, 1829–1844. [CrossRef]

46. Kaur, J.; Vergara, A.; Rossi, M.; Gravagnuolo, A.M.; Valadan, M.; Corrado, F.; Conte, M.; Gesuele, F.; Giardina, P.; Altucci, C. Electrostatically driven scalable synthesis of MoS$_2$–graphene hybrid films assisted by hydrophobins. *RSC Adv.* **2017**, *7*, 50166–50175. [CrossRef]

47. Wang, Y.; Tang, X.; Liu, Z.; Liu, Z.; Yan, Y.; Yang, B.; Zhu, Z. Fabrication of a Z-scheme MoS$_2$/CuO heterojunction for enhanced 2-mercaptobenzothiazole degradation activity and mechanism insight. *New J. Chem.* **2020**, *44*, 18264–18273. [CrossRef]

48. Li, Z.; Pi, Y.; Xu, D.; Li, Y.; Peng, W.; Zhang, G.; Zhang, F.; Fan, X. Utilization of MoS$_2$ and graphene to enhance the photocatalytic activity of Cu$_2$O for oxidative CC bond formation. *Appl. Catal. B Environ.* **2017**, *213*, 1–8. [CrossRef]

49. Zhong, X.; Royer, S.; Zhang, H.; Huang, Q.; Xiang, L.; Valange, S.; Barrault, J. Mesoporous silica iron-doped as stable and efficient heterogeneous catalyst for the degradation of C.I. Acid Orange 7 using sono–photo-Fenton process. *Sep. Purif. Technol.* **2011**, *80*, 163–171. [CrossRef]